

# Facile Synthesis of Hierarchical Iron Phosphide/Biomass Carbon Composites for Binder-Free Sodium-Ion Batteries

Hui Wu,<sup>[a]</sup> Xueying Li,\*<sup>[a]</sup> Lizhuang Chen,<sup>\*[a]</sup> and Yuanyuan Dan<sup>[a]</sup>

Seeking a simple direct construction strategy for transition-metal-phosphide-based composites as anodes for sodium-ion batteries is attracting great attention for the development of high-performance sodium-ion batteries. In this work, we design iron phosphide nanosheets grown on a biomass carbon membrane by a facile electrodeposition method, followed by an annealing process. The biomass carbon membranes as three dimensional frameworks, possessing initial biological structures from Magnolia leaves, do not only improve the conductivity of the electrodes but also relieve iron phosphide aggregation

during the charging-discharging processes. The iron phosphide nanosheets could increase the accessible surface area for electrochemical reactions, further promoting the storage of sodium ions. Due to the unique structure of the iron phosphide nanosheets/biomass carbon membrane, the electrodes exhibit  $500.9 \text{ mAh g}^{-1}$  at a current density of  $50 \text{ mA g}^{-1}$  after 100 cycles. Even at a high current density of  $500 \text{ mA g}^{-1}$ , the electrodes still retain  $197 \text{ mAh g}^{-1}$  after a long-time test (500 cycles). These novel features make the composite a great potential anode material for binder-free sodium-ion batteries.

## 1. Introduction

Limited reserves of lithium in earth make the lithium ion batteries (LIBs) hard to meet the demand for electronic device market, especially for large-scale applications. Sodium is adjacent to lithium in the periodic table of elements, owing the similar chemical and physical properties. Because of the great global abundance of Na in earth and analogous energy storage mechanism, sodium ion batteries are considered as a potential alternative for lithium ion batteries. However, the large radius of  $\text{Na}^+$  (55% larger than that of  $\text{Li}^+$ ) results in sluggish sodium ion transfer and large volume fluctuation during charge/discharge processes.<sup>[1–7]</sup>

More attentions have been focused on developing high-efficient anode material with excellent electrochemical performance and low cost.<sup>[8–13]</sup> Among various high-efficient anode materials for Na storage, transitional metal phosphides have unique physical properties and electrochemical characteristics in energy storage and electro catalysis, due to the existence of multi-electron orbitals.<sup>[14–18]</sup> Transitional metal phosphides as anode materials have relatively low redox potential result in a full cell with a high output voltage. Such as tin phosphides, iron phosphides, and several other metal phosphides are all electrochemically active in sodium ion batteries.<sup>[19–27]</sup> It is known that these phosphides react with sodium to form the  $\text{Na}_3\text{P}$ , and therefore have high theory capacities. The accompanying mechanical strain will deteriorate the integrity of electrode, block electronic channels and peel off active materials from

current collector, thus giving rise to a serious capacity fading during sodiation/desodiation processes.

To address the problems, researchers utilize the carbon material to improve the nanostructures of transitional metal phosphides.<sup>[28–31]</sup> The nanocomposites of carbon materials were verified to be facilitated to alleviate the pulverization of transitional metal phosphides, keep the structure stability and promote the electronic conductivity during cycling. Han et al.<sup>[32]</sup> synthesized two-phase of carbon modified amorphous iron phosphide with well-developed mesoporous structure by nanoconfinement reaction method. The composites delivered a sodium-ion storage capacity of  $415 \text{ mAh g}^{-1}$  at the current density of  $100 \text{ mA g}^{-1}$ . When the current density reached  $500 \text{ mA g}^{-1}$ , the capacity was still above  $300 \text{ mAh g}^{-1}$ . In those carbon materials, biomass carbon could provide environmental friendly hard carbon precursor for sodium ion anodes due to the low cost and mass production.<sup>[33]</sup> Several biomass,<sup>[34]</sup> such as peat moss,<sup>[35]</sup> lobster shell,<sup>[36]</sup> cellulose nanofiber,<sup>[37]</sup> strew,<sup>[38]</sup> and holly leaf<sup>[39]</sup> have been used as biomass carbon precursors. The derived biomass carbons as hard carbons possess short range turbo static structures, which is beneficial to the sodium storage. Typically, Li et al.<sup>[40]</sup> prepared carbon membrane from oak leaf by one-step thermal pyrolysis route. The carbonized leaf membrane as a binder-free anode exhibited the specific capacity of  $360 \text{ mAh g}^{-1}$ . And some other carbon/metal sulfides or oxides binder-free electrodes in the Na ion battery also exhibited more excellent performance in early works.<sup>[41,42]</sup>

We attempted to fabricate hierarchical iron phosphide grown on biomass carbon membranes by a facile electrodeposition method to promote the cyclability of iron phosphides based anode materials for sodium ion batteries. The hierarchical iron phosphide could be fully exposed to electrolyte to provide plenty of reactive sites for sodium ion storage. The porous biomass carbon membranes used as a current collector not only relax the mechanical stress of iron phosphides but also facilitate the electron conduction. Thereby, the

[a] H. Wu, Dr. X. Li, Prof. L. Chen, Dr. Y. Dan  
School of Environmental and Chemical Engineering, Jiangsu University of  
Science and Technology  
Zhenjiang, 212003, China  
E-mail: Lixueying@just.edu.cn  
clz1977@sina.com

 Supporting information for this article is available on the WWW under  
<https://doi.org/10.1002/batt.201800113>

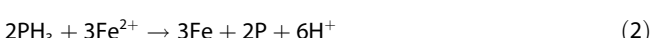
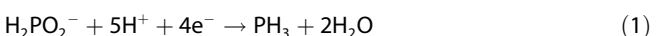
binder-free composite electrode exhibited enhanced specific capacity and cyclability during the charge/discharge processes.

## 2. Results and Discussion

As illustrated in Figure 1a, the IPs/BC composite has been successfully synthesized mainly through a facile electrodeposition on the biomass carbon. The natural magnolia leaf turns black after carbonization at 800°C under N<sub>2</sub>, indicating successful transformation into biomass carbon. It is worth to notice that the biomass carbon membrane inherits the natural morphology of the biomass precursor. The pores and nanofibers on the surface of carbon membrane can be identified obviously in the Figure 1b. The internal structure of carbon membranes with good honeycombing pattern own good mechanical properties, showing in the SEM image of the cross-section part in Figure 1c. The total thickness of cross-sectional portion is about 150 μm. The highly porous in the carbonized leaf is similar to the biomass carbon membrane with the other leaf as hard template. The unique structure exhibited great advantages as diffusion network. The pores and interior honeycombing pattern can significantly increase the wettability and promote the ion transport. The fibers on the surface of carbon membrane and the whole carbon network facilitate the electron passport. The synergistic effects of different structures can improve rate capacity and cyclability.

Moreover, there are many functional groups at the nanofibers of carbonized leaf, which can provide sufficient active

surface sites to combine iron phosphide nanoparticles. After a simple electrodeposition process, the iron phosphide nanosheets have been grown on the surface of the carbonized leaves to form IPs/BC. According to the references,<sup>[43–46]</sup> the electrodeposition of iron phosphide involves three reactions as follows:



The reduced Fe and reduced P are combined in the iron phosphides on the surface of electrode during the electrodeposition.

However, the morphology is different from other iron phosphides obtained by electrodeposition,<sup>[46]</sup> which is due to the influence of substrate materials. As seen from the Figure 1d and e, the morphology of hierarchical iron phosphides on the carbon membrane is strongly dependent on the electrodeposition time. At the beginning of the electrodeposition (1 min), only a few of scattered nanoflakes can be found on the surface of carbon membrane in Figure 1d. When the electrodeposition time got to 30 minutes, the iron phosphide nanosheets uniformly distributed at the nanofibers on the surface of biomass carbon membrane can be seen clearly in the Figure 1e. The internal carbon membrane also be filled with the iron phosphides (Figure S1†).

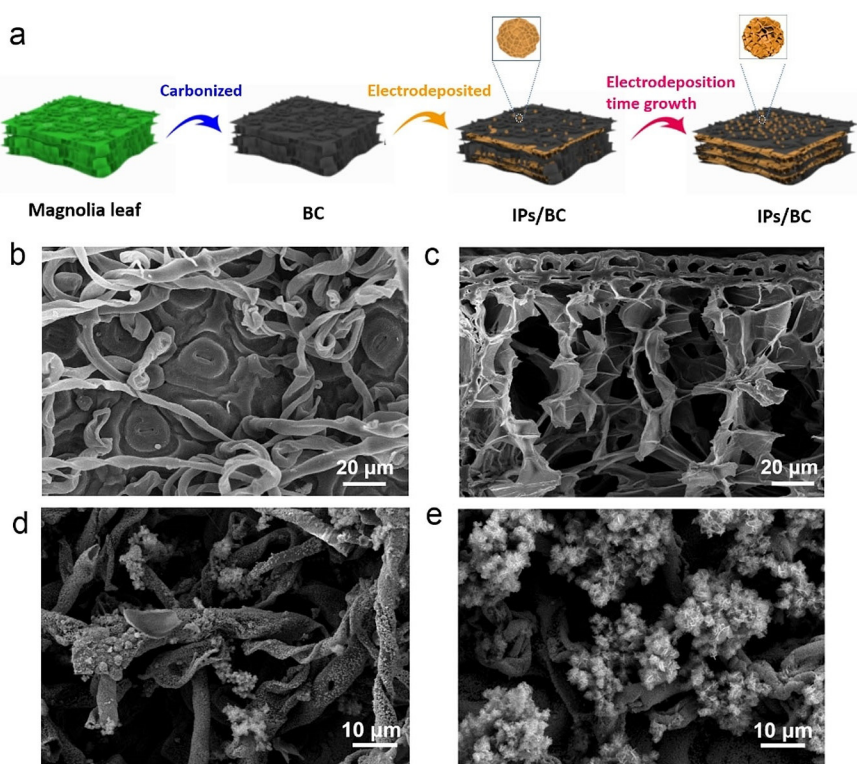


**Figure 1.** a) Schematic illustration of the synthesis of the IPs/BC composite. SEM images of: b) the surface portion of BC and c) the cross-sectional portion of BC. d) Electrodeposited IPs/BC composite after 1 min. e) Electrodeposited IPs/BC composite after 30 minutes.

To further investigate the structural evolution of the iron phosphide nanosheets on biomass carbon membrane during the electrodeposition processes. The growth process of iron phosphides were observed by field-emission scanning electron microscopy (FESEM) at different deposition times, as shown in Figure 2. At the beginning of electrodeposition process (1 min), the iron phosphides nanoflakes are formed at the surface of nanofiber on the carbon membrane with the thickness of 10–20 nm and the size of 600–800 nm. The nanoflakes gradually become thinner and larger for growth periods varying from 5 min to 30 min (Figure 2b–d), attributing to the deposition effect and accompanying selective dissolution of Fe and Fe-rich phase in the electrolyte. Finally, the nanoflakes transform into the nanosheets, being uniformly distributed at the nanofibers on the surface of biomass carbon membrane (Figure 2d). The inset TEM images could further demonstrate the nanosheets hierarchical structure is successfully obtained. The morphology of annealing films is similar with the as-prepared electrodeposition films (Figure S2†). The specific surface areas and porous structures of BC and IPs/BC composites are characterized by the  $N_2$  absorption-desorption isotherm (Figure S3†). The

calculated Brunauer-Emmett-Teller (BET) surface area of BC and IPs/BC composites are  $140.03\text{ m}^2\text{ g}^{-1}$  and  $137.8\text{ m}^2\text{ g}^{-1}$ , respectively. The Barrett-Joyner-Halenda (BJH) pore size distribution curves (Figure S3† inset) show that the range of pore size in the IPs/BC composites is mainly between 3 nm–10 nm, which is little wider than that in BC (3 nm–8 nm). Figure 2e shows microscopic image of the carbon membrane electrodeposited with iron phosphide. It is clearly seen the whole deposition film is very uniform. The element mapping analysis was used to further demonstrate the distribution of elements in the IPs/BC composite. The Fe, P, C and O elements are uniformly distributed in the composites, confirming a homogenous iron phosphide films on the biomass carbon membrane. The element is from the partial oxidation at the surface of iron phosphide films caused from the sample exposed in air. The iron phosphides nanosheets in the composite are facilitate for the infiltration of electrolyte. The porous carbon membrane as current collector and conductive carbon network is beneficial for enhanced sodium storage.

The structure information of as-prepared electrodeposited IPs/BC and annealed IPs/BC are confirmed by XRD. Figure 3a

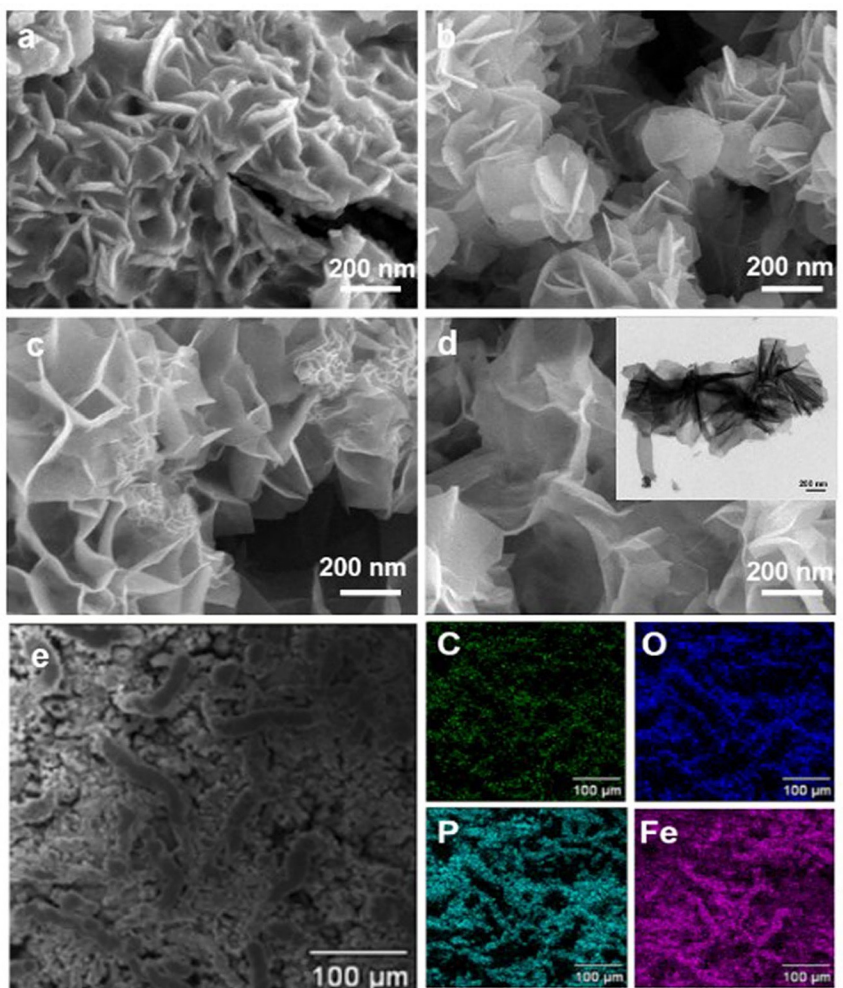


**Figure 2.** SEM images of IPs/BC composites at different electrodeposition times: a) 1 min; b) 5 min; c) 10 min; and d) 30 min (inset TEM image). e) Element mapping images of C, O, P and Fe.

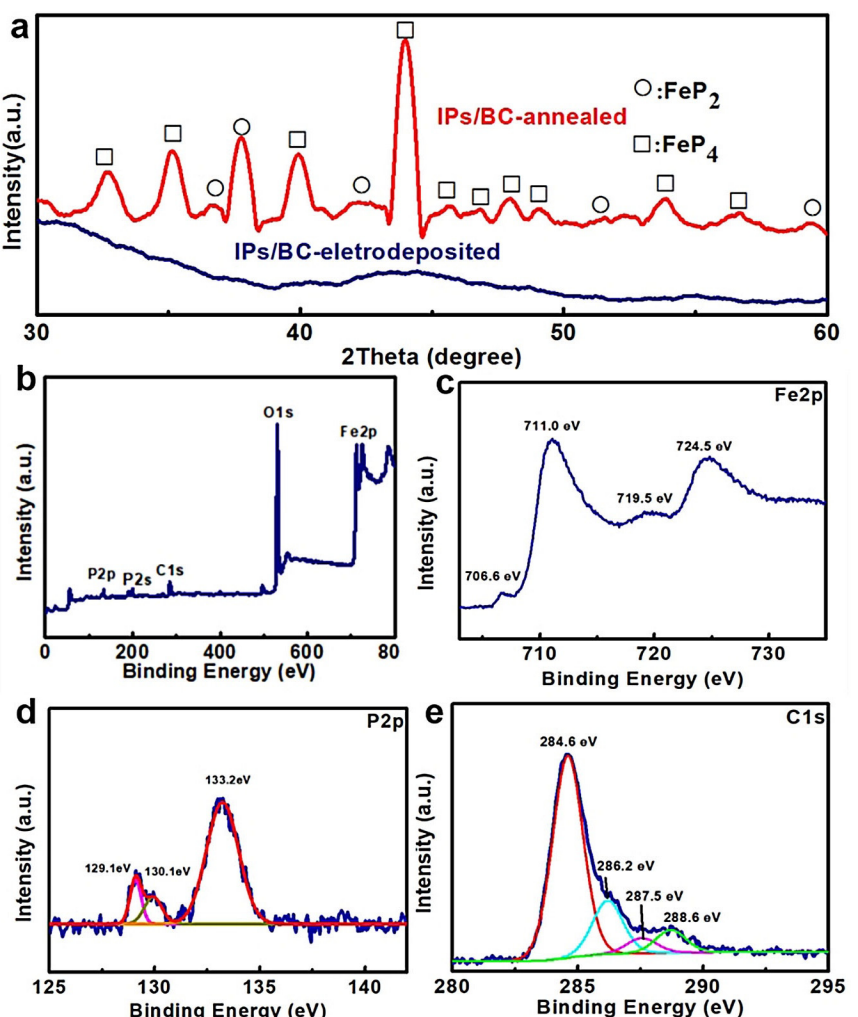


**Figure 3.** a) XRD patterns of IPs/BC composites. b) XPS survey spectrum of the IPs/BC composite and high-resolution XPS spectra of: Fe 2p (c), P 2p (d) and C 1s (e).

shows XRD patterns of the electrodeposited IPs/BC composites and annealed IPs/BC composites. Obviously, there is a wide diffraction peak in the XRD pattern of electrodeposited IPs/BC, which confirmed the amorphous films formed on the biomass carbon membrane during electrodepositing process. After annealing at 300 °C for 1 h, the IPs/BC composites exhibits superior crystallization. The peaks at 36.5°, 37.6°, 40.9°, 52.3°, 59.5° can be assigned to (011), (101), (111), (211), (031) planes of orthorhombic phase FeP<sub>2</sub> (JCPDS no.71-2234). The other diffraction peaks are fitted with related planes of orthorhombic phase FeP<sub>4</sub> (JCPDS no.71-0482). Thereby, the IPs/BC composites are the mixed phase contained FeP<sub>2</sub>, FeP<sub>4</sub> after annealing process. Analyzed from XRD patterns, the iron phosphides in the composites are composed of 31% FeP<sub>2</sub> and 69% FeP<sub>4</sub>. The result is similar with the other works referred the electrodeposition of iron phosphides.<sup>[44,46,47]</sup>

X-ray photoelectron spectroscopy (XPS) is used to characterize the surface characteristics of IPs/BC. The peaks corresponding to P, C, O, Fe element are observed in the survey scan spectrum of IPs/BC electrode (Figure 3b), coincide with the element mapping results. The high-resolution Fe 2P in the

Figure 3c shows that four peaks located at 706.6 eV, 711.0 eV, 719.5 eV and 724.5 eV, respectively. The main peaks at 711.0 eV and 724.5 eV are corresponded to the electron binding energy for Fe in iron phosphides.<sup>[15]</sup> The satellite peak of 719.5 eV belongs to the characterization of Fe<sup>3+</sup>.<sup>[29]</sup> The peak with binding energy value of 706.6 eV is assigned to the Fe<sup>0</sup> 2p from the reduction during electrodeposition process. High-resolution XPS spectra of P 2p for IPs/BC electrode is showed in the Figure 3d. Two peaks at 129.1 eV and 130.1 eV are ascribed to the binding energy for P in IPs/BC.<sup>[48]</sup> Furthermore, the peak at 133.2 eV can be attributed to the superficial oxidation of P species in iron phosphides exposed to air.<sup>[49]</sup> The high-resolution XPS spectrum of C 1s shows four fitted peaks at 284.6 eV, 286.2 eV, 287.5 eV, 288.6 eV, which are attributed to sp<sup>2</sup> hybridized graphitic C atoms, C—O species, C=O, and O=C=O (Figure 3e).<sup>[50]</sup>

The electrochemical performance of IPs/BC composite has been studied as anodes for sodium-ion batteries (SIBs) without binder and conductive additive. Figure 4a presents the initial three cyclic voltammogram curves of BC membrane and IPs/BC composite films between 0.01 V and 3.0 V. The voltammetric

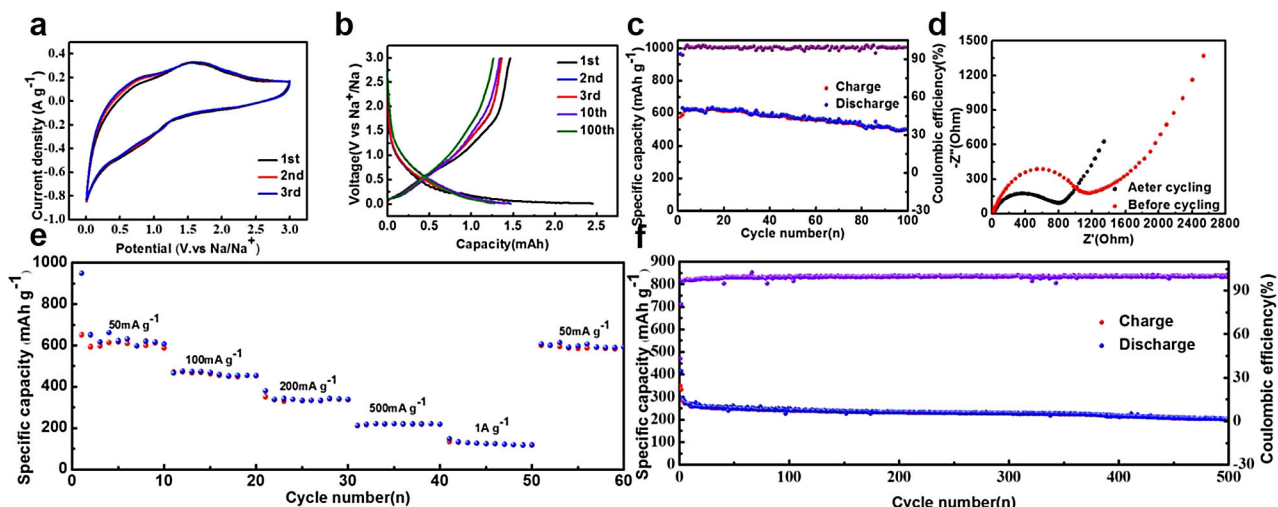


**Figure 4.** Sodium-storage properties of the IPs/BC electrodes: a) CV curves at a scan rate of  $0.1 \text{ mV s}^{-1}$ ; b) discharge-charge curves at  $50 \text{ mA g}^{-1}$ ; c) cycling performance of the IPs/BC electrodes at  $50 \text{ mA g}^{-1}$ ; d) Nyquist plots of the IPs/BC electrodes before (red curve) and after (black curve) cycling with the fitted equivalent circuit inset; e) rate capabilities of IPs/BC; f) cycling performances of the IPs/BC electrodes at  $500 \text{ mA g}^{-1}$ .

profiles of IPs/BC composite films are similar to the sodium storage of iron phosphides. The redox peaks at  $0.75 \text{ V}$  and  $1.6 \text{ V}$  are response for the typical sodium-ion insertion and extraction of iron phosphides. The board cathodic peak is due to the difficult sodium insertion into the IPs/BC composite films. In the subsequent cycles, the anodic peak at  $0.6 \text{ V}$  is increasing with the cycling, which is attributed to the electrochemical activation during the insertion/extraction processes. Notably, the redox peaks keep at the same position in voltammetric profiles of three cycles, indicating the excellent cyclability of the sodium storage reaction in the IPs/BC composite. The discharge-charge curves of IPs/BC composite for the 1st, 2nd, 3th, 10th and 100th cycles at current density of  $50 \text{ mA g}^{-1}$  are shown in Figure 4b. The sodium insertion/extraction potential in the IPs/BC composite is respectively around  $0.5 \text{ V}$  and  $1.5 \text{ V}$ , which is in good agreement with the cyclic voltammetry curves. Because the electrochemical active material is mixed phase, showing in the XRD pattern, the plateaus of charge and discharge at different cycling are inconspicuous. The increase of cycle number results in the electrochemical polarization, in terms of higher discharge and charge potentials. Overall, the discharge-charge profiles of IPs/BC composites with different cycles have the similar shapes, which imply the electrode materials can keep the structural stability. The total weight of electrode materials is about  $4.5 \text{ mg}$ , the weight of carbon materials is about  $2.5 \text{ mg}$ . In order to estimate the capacity contribution of biomass carbon membrane in the IPs/BC composites, the discharge-charge profiles of biomass carbon membranes with the same mass as well as that in the composites are tested at the same current density (Figure S4†). Similar with the most biomass carbon as anode for sodium ion batteries, the plateau of sodiation/desodiation reaction is below the  $0.20 \text{ V}$ .<sup>[51,52]</sup> As seen in the Figure S4†, although the first discharge capacity is  $205 \text{ mAh g}^{-1}$ , the reversible capacity is only about  $70 \text{ mAh g}^{-1}$ . Thereby, the capacity contribution of biomass carbon has been eliminated in

the following tests. Thereby, the following calculation of specific capacity is based on the mass of iron phosphides.

The cycling stability and coulombic efficiency of IPs/BC composites at  $50 \text{ mA g}^{-1}$  are shown in Figure 4c. It is noteworthy that the reversible specific capacity of IPs/BC composites is much larger than that of BC electrodes (Figure S5†). The superior capacity is attributed to the plenty of  $\text{Na}^+$  storage active sites in the iron phosphide nanosheets. It presents the first discharge specific capacity of  $964.3 \text{ mAh g}^{-1}$  with an initial coulombic efficiency of  $59.72\%$ . The lower initial coulombic efficiency may be resulted from the porous structure of biomass carbon membrane and large surface area of nanosheets leading excessive consumption of the electrolyte to form SEI films. As seen in the cycling performance curves with the following cycles, the discharge and charge capacities of the 2nd cycle are  $588.2$  and  $631.8 \text{ mAh g}^{-1}$  with coulombic efficiency increases dramatically to  $93.09\%$  (Figure 4c). After the 100<sup>th</sup> cycles, the discharge capacity of IPs/BC composites is still maintained at  $500.9 \text{ mAh g}^{-1}$  with the coulombic efficiency around  $99.11\%$ . The corresponding reversible areal capacity is about  $1.5 \text{ mAh cm}^{-2}$  (Figure S6†). The phenomenon of IPs/BC composites is similar with the other iron phosphide/carbon composites at the same current density.<sup>[48–50]</sup> The superior specific capacity and stable cyclability are outstanding compared to the other previously reported related iron phosphides based anode materials (Table S1). It is noteworthy that the iron phosphide loading mass in the IPs/BC is relatively high in those works. Normally, the high loading mass of iron phosphides could impede the electrochemical performance, but IPs/BC binder-free electrodes still have high specific capacity and good cyclability. In order to further investigate the structural stability of IPs/BC composites, the morphology of IPs/BC composites after cycling at the current density of  $50 \text{ mA g}^{-1}$  were investigated (Figure S7†). As seen from the SEM image, although the iron phosphide nanosheets suffered from the stress variation damage, the hierarchical surface of IPs/BC composites is still

visible. The iron phosphide nanosheets attached on the biomass carbon membrane is still retained.

To better elucidate the charge transfer kinetics of IPs/BC composites, electrochemical impedance spectroscopy (EIS) measurements were performed before the first cycle and after 100 cycles completely charge-discharge cycling at  $50 \text{ mA g}^{-1}$ . The Nyquist plot consists of a wide semicircle in the high-frequency to intermediate-frequency region, followed by a slope line in the low frequency region, as shown in the Figure 4d. The EIS data were further fitting by equivalent circuit (Figure 4d inset). The intercept of semicircle in the high-frequency region represents ohmic resistance ( $R_s$ ), which is assigned to sodium ion transportation in the electrolyte. The wide semicircle in the high-middle frequency range could be fitted by two overlapping semicircles. The semicircle in the high-frequency range corresponds to the migration and charge transfer of SEI layer resistance ( $R_t$ ), accompanied by the dielectric capacitance (CPE) of interface between electrolyte and electrode materials. The semicircle in the middle-frequency range refers to the charge transfer resistance ( $R_{ct}$ ) of the IPs/BC composites. It is clearly seen the  $R_{ct}$  of IPs/BC is reduced from  $871.9 \Omega$  to  $644.6 \Omega$ . It is inferred the hierarchical structure of the IPs/BC could preserve the charge transfer channel and maintain the initial morphology. The sloping line represents the diffusion process of sodium ions in the bulk materials, Warburg impedance ( $Z_{\text{diff}}$ ). The similar slope of straight line in those two curves verifies the capability of sodium ion diffusion in the electrode after cycling as well as before the first cycle.

The rate capability of IPs/BC composites was evaluated at various current densities of  $50 \text{ mA g}^{-1}$ ,  $100 \text{ mA g}^{-1}$ ,  $200 \text{ mA g}^{-1}$ ,  $500 \text{ mA g}^{-1}$  and  $1 \text{ A g}^{-1}$  as presented in Figure 4e. Apparently, the reversible capacities decrease regularly with the increasing current densities. The high-rate capacities of  $612.5$ ,  $452.7$ ,  $337.5$ ,  $265.6$ , and  $117.9 \text{ mAh g}^{-1}$  can be obtained at rates of  $50 \text{ mA g}^{-1}$ ,  $100 \text{ mA g}^{-1}$ ,  $200 \text{ mA g}^{-1}$ ,  $500 \text{ mA g}^{-1}$  and  $1 \text{ A g}^{-1}$ , respectively. The poor performance of IPs/BC at high current density is related to the slower ion transfer in the IPs/BC composites. The reversible capacity is still retained to  $590.6 \text{ mAh g}^{-1}$  after the current density is back to  $50 \text{ mA g}^{-1}$ . Thus, the IPs/BC electrode demonstrates a superiority rate performance.

Moreover, the IPs/BC electrode also displays an attractive long-term cyclability at a current density of  $500 \text{ mA g}^{-1}$  (Figure 4f). The IPs/BC electrode delivers a slight decay with reversible capacity of  $197 \text{ mAh g}^{-1}$  after 500 cycles, accompanying with the coulombic efficiency of 99.54%. Such stable cycling capability at high current density is superior to most of previously reported iron phosphides based anode materials for sodium ion batteries.<sup>[7,16,53,54]</sup>

The obtained data clearly demonstrate the superior sodium storage performance of IPs/BC electrode for sodium ion batteries can be attributed to the unique three-dimensional structure. As presented in Figure 5, the iron phosphides nanosheets not only facilitate the sodium ion transportation to provide more active sites for sodium storage but also relax the volume variation stress of iron phosphides during discharge/charge process. Meanwhile, the biomass carbon membrane as conductive carbon network can enhance the electronic con-

ductivity of electron transfer for reaction kinetics. Secondly, the whole three-dimensional structure can prevent the aggregation of iron phosphide to improve the structural stability, achieving long-term cyclability. Thirdly, the porous structure in the biomass carbon membrane is beneficial for infiltration of electrolyte into the active material ensure fast electron transportation and ion diffusion.

The cyclic voltammetry at different scan rates for  $0.2 \sim 1.0 \text{ mV s}^{-1}$  in Figure 5b can further demonstrate the capacitive effect in the battery system. The charge storage mechanism includes sodium ion intercalation process and surface capacitive contribution. The capacitive effect could be estimated from the CV curves at different scan rates as following equation:

$$\ln I(V) = b^* \ln \nu + \ln a$$

Which describe the linear relationship between the current densities ( $I(V)$ ) of peak voltage( $V$ ) and the scan rates( $\nu$ ).<sup>[55,56]</sup> The  $b$  value as slope of the curve can provide the sodium storage mechanism. When the value of  $b$  is near to 0.5, sodium ion diffusion-controlled process dominates in capacitive contribution. If the  $b$  value is close to 1, the total capacitance mainly comes from the surface capacitive. Figure 5c shows the  $\ln I(V)$  versus  $\ln \nu$  at different peaks of IPs/BC electrodes. The  $b$  values of the oxidation and reduction peaks are above 0.77, which indicate the capacitance contribution is mainly from the surface capacitance. In order to further investigate the specific capacitance contribution of surface capacitance effect and sodium ion diffusion-controlled process. Dunn et al.<sup>[57]</sup> proposed an important method to separate the current into capacitive current ( $k_1 \nu$ ) and diffusion-controlled current ( $k_2 \nu^{1/2}$ ) based on the given equation:

$$I(V) = k_1 \nu + k_2 \nu^{1/2}$$

The  $I(V)$  means the total current at given voltage,  $\nu$  represents the scan rate. After arranged the equation and plotted the  $I(V)/\nu^{1/2}$  vs.  $\nu^{1/2}$ , we could obtain the  $k_1$  and  $k_2$  value and further calculate the capacitance contribution at different voltages, shown in the Figure 5d. The surface capacitances increase from 45.9% to 67.9% with the rising scan rates. The phenomenon reveals the rate of charge transfer positively effect on the surface capacitance. The surface capacitance is benefit for fast charge transfer and long cycling. Figure 5e shows the pseudocapacitive contribution is about 59.6% in the total charge storage at the scan rate of  $0.6 \text{ mV s}^{-1}$ . The result is agreement with the  $b$  values. The iron phosphide nanosheets could facilitate surface capacitance in the electrochemical process at high current density.

### 3. Conclusions

In summary, we fabricated the hierarchical iron phosphides / biomass carbon by a facilitate electrodeposition method. Iron phosphide nanosheets are uniformly grown on the nanofiber on the surface of biomass carbon membrane. The nanosheets

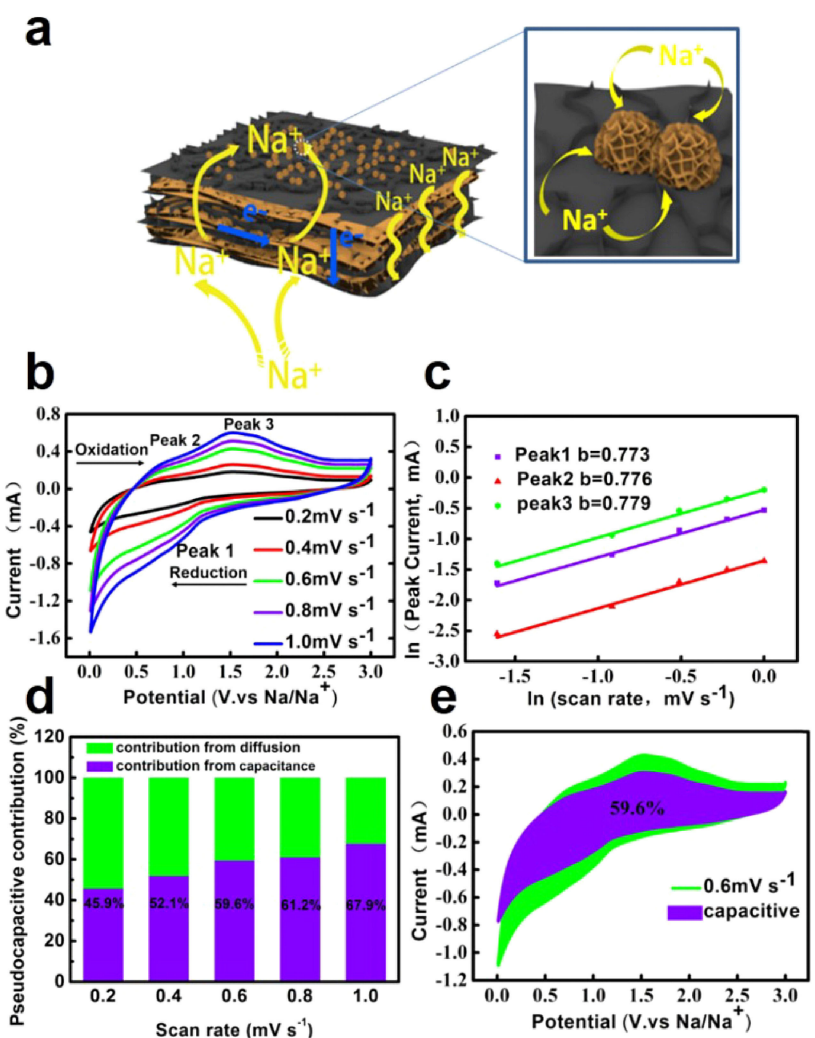


**Figure 5.** a) Schematic illustration of the transport paths of  $\text{Na}^+$  and electrons in the IPs/BC electrode. b) CV curves of IPs/BC at different scan rates. c)  $\ln I$  versus  $\ln v$  plots at different anodic peaks and cathodic peaks. d) Diffusion-controlled processes (green region) and capacitive (violet region) contribution to the charge storage of IPs/BC. e) Capacitive (violet region) contribution to the charge storage of IPs/BC at 0.6  $\text{mV s}^{-1}$ .

structure is beneficial for enhancing the specific surface areas to access sodium ions and shorten the ion diffusion path. Meanwhile, the interconnected porous structure in the biomass carbon membrane not only confines the iron phosphide but also promote the conductivity of whole electrodes for fast electrochemical reactions. The unique hierarchical structures result in the electrodes exhibit a reversible specific capacity of  $500.9 \text{ mAh g}^{-1}$  at low current density of  $50 \text{ mA g}^{-1}$ . Besides, the composites could suffer higher current density of  $500 \text{ mA g}^{-1}$  and still retain  $197 \text{ mAh g}^{-1}$  after long-term cycling. The achieved results clearly verify the synergistic effect between iron phosphides and biomass carbon membrane could be utility in the high performance and low-cost anode materials for sodium ion batteries.

## Experimental Section

### Synthesis of Biomass Carbon Membrane (BC)

The Magnolia leaf was treated by ethanol before been tailored into square in order to remove the dust. The leaf was pressed on graphite slide then load in a tube furnace and carbonized at  $800^\circ\text{C}$  for 2 h in  $\text{N}_2$  with the heating rate of  $3^\circ\text{C min}^{-1}$ . After the sample cooling down, the carbonized leaf membrane was placed in 2 M HCl aqueous solution at  $60^\circ\text{C}$  for 12 h, and then they were immersed in 2 M KOH solution and kept at  $70^\circ\text{C}$  for 2 h. Finally, the carbonized membrane was washed to neutrality and dried at  $70^\circ\text{C}$  overnight.

### Synthesis of Iron Phosphide/Biomass Carbon Membrane (IPs/BC)

For electrochemical deposition experiments, a square carbonized leaf membrane was pasted on copper plate. Then the assembled electrode was immersed to the electrolyte, which contained 0.7 M  $\text{FeSO}_4 \cdot 7\text{H}_2\text{O}$ , 0.4 M  $\text{NaH}_2\text{PO}_4$ , 0.11 M  $\text{H}_2\text{NCH}_2\text{COOH}$  and 5 mM

$\text{H}_2\text{C}_2\text{O}_4$  in the sealed electrolytic cell. The pH of mixed solution was adjusted to 2.3 by adding  $\text{H}_2\text{SO}_4$ . The Pt foil was used as the counter electrode. The reference electrode was Ag/AgCl electrode. Iron phosphides was directly electrodeposited on the carbon membranes at room temperature ( $25^\circ\text{C}$ ) by potentiostatic methods at a constant applied voltage ( $-1.5\text{ V}$ ) for 30 min in the sealed electrolytic cell. The off-gas was treated by  $\text{KMnO}_4$  aqueous solution. Each obtained sample was put into a tubular furnace at  $300^\circ\text{C}$  for 1 h by the heating rate of  $1^\circ\text{C min}^{-1}$  in nitrogen protection. The samples were collected after cooling to room temperature ( $25^\circ\text{C}$ ) for subsequent materials characterization and performance test.

## Materials Characterization

The morphologies of the biomass carbon membranes and iron phosphides/carbon composites were observed by field emission scanning electron microscopy (FESEM, JSM-7600F). Compositions of the samples were investigated by Oxford X-Max energy dispersive spectrometer (EDS). The powder X-ray diffraction (XRD) measurements were taken on a Bruker D8 Advance X-ray diffractometer with  $\text{Cu K}\alpha$  radiation ( $\lambda=1.5418\text{ \AA}$ ). The Brunauer-Emmett-Teller (BET) analysis for  $\text{N}_2$  adsorption-desorption isotherms were performed on a Micromeritics ASAP2020 instrument. X-ray photoelectron spectroscopy (XPS) data were collected on an Perkin-Elmer model PHI 5600 X-ray photoelectron spectrometer with  $\text{Al K}\alpha$  X-ray as the excitation source. All XPS profiles were calibrated based on a C 1s binding energy of 284.6 eV.

## Electrochemical Measurement

The electrochemical behavior of iron phosphides /biomass carbon (IPs/BC)( $0.8\text{ cm} \times 0.8\text{ cm}$ ) was conducted with CR2032 coin-type cells. The cells were assembled in the Ar filled glove box with sodium metal as both the reference electrode and counter electrode, whatman glass microfiber (CAT No.1820-047) as the separator, 1 M  $\text{NaClO}_4$  in ethylene carbonate (EC)-diethyl carbonate (DEC) (1:1 in volume) and 5 wt% fluoroethylene carbonate (FEC) as the electrolyte. The cyclic voltammetry (CV) curves were recorded on a CHI-760E workstation between 0.01–3 V at a scanning rate of  $0.5\text{ mVs}^{-1}$ . Electrochemical impedance spectroscopy (EIS) was tested by the Autolab PGSTAT302N potentiostat (Eco-Chemie) with a frequency range of 100 KHz to 0.01 Hz at  $5\text{ mVs}^{-1}$ . The galvanostatic cycle performances of cells were performed between 0.01–3.0 V vs.  $\text{Na}^+/\text{Na}$  using a battery test system (LAND CT-2001A) at room temperature ( $25^\circ\text{C}$ ).

## Acknowledgements

This work was supported partially by the National Natural Science Foundation of China (NSFC, No. 21671084, 51502117), Natural Science Foundation of Jiangsu Province (No. BK20180983), Key Research & Developement Plan of Zhenjiang City (No. SH2017051), and the Natural Science Foundation of the Jiangsu Higher Education Institution of China (No. 18KJB480004). We thank Dr Hu Zhou at the Instrument Analysis Center of Jiangsu University of Science and Technology for his assistance with SEM.

## Conflict of Interest

The authors declare no conflict of interest.

**Keywords:** anodes · binder-free electrode · biomass carbon · iron phosphides · sodium-ion battery

- [1] B. Dunn, H. Kamath, J. M. Tarascon, *Science* **2011**, *334*, 928–935.
- [2] S. Y. Hong, Y. Kim, Y. Park, A. Choi, N. S. Choi, K. T. Lee, *Energy Environ. Sci.* **2013**, *6*, 2067–2081.
- [3] M. D. Slater, D. Kim, E. Lee, C. S. Johnson, *Adv. Funct. Mater.* **2013**, *23*, 947–958.
- [4] F. Li, Z. Zhou, *Small* **2018**, *14*, 1702961.
- [5] V. Palomares, P. Serras, I. Villaluenga, K. B. Hueso, J. Carretero-González, T. Rojo, *Energy Environ. Sci.* **2012**, *5*, 5884–5901.
- [6] L. Hu, X. Hu, Z. Lin, Z. Wen, *ChemElectroChem* **2018**, *5*, 1552–1558.
- [7] Z. Li, L. Zhang, X. Ge, C. Li, S. Dong, C. Wang, L. Yin, *Nano Energy* **2017**, *32*, 494–502.
- [8] N. Yabuuchi, K. Kubota, M. Dahbi, S. Komaba, *Chem. Rev.* **2014**, *114*, 11636–11682.
- [9] X. Y. Li, L. Z. Chen, Y. Y. Qu, Y. Y. Ma, *Sustainable Energy Fuels.* **2018**, *2*, 1124–1140.
- [10] X. Y. Li, Y. Y. Ma, G. Z. Cao, Y. Y. Qu, *J. Mater. Chem. A* **2016**, *4*, 12487–12496.
- [11] J. Zhang, M. Huang, B. Xi, K. Mi, A. Yuan, S. Xiong, *Adv. Energy Mater.* **2018**, *8*(2): 20170133.
- [12] L. Zou, Y. Q. Lai, H. X. Hu, M. R. Wang, K. Zhang, P. Zhang, J. Fang, J. Li, *Chem. Eur. J.* **2017**, *23*, 14261–14266.
- [13] J. Gao, Y. Li, L. Shi, J. Li, G. Zhang, *ACS Appl. Mater. Interfaces* **2018**, *10*, 24, 20635–20642.
- [14] J. Li, L. Shi, J. Gao, G. Zhang, *Chem. Eur. J.* **2018**, *24* (6), 1253–1258.
- [15] D. Li, Q. Liao, B. Ren, Q. Jin, H. Cui, C. Wang, *J. Mater. Chem. A* **2017**, *5*, 11301–11308.
- [16] M. Huang, K. Mi, J. Zhang, H. Liu, T. Yu, A. Yuan, Q. Kong, S. Xiong, *J. Mater. Chem. A* **2017**, *5*, 266–274.
- [17] K. Zhang, M. Park, J. Zhang, G. H. Lee, J. Shin, Y. M. Kang, *Nano Res.* **2017**, *10*, 4337–4350.
- [18] J. J. Li, L. Shi, J. Y. Gao, G. Q. Zhang, *Chem. Eur. J.* **2018**, *24*, 1253–1258.
- [19] J. W. Hall, N. Membruno, J. Wu, H. Celio, R. A. Jones, K. J. Stevenson, *J. Am. Chem. Soc.* **2012**, *134*, *12*, 5532–5535.
- [20] R. Mogensen, J. Maibach, A. J. Naylor, R. Younesi, *Dalton Trans.* **2018**, 10752–10758.
- [21] D. Zhou, L. Z. Fan, *J. Mater. Chem. A* **2018**, *6*, 2139–2147.
- [22] S. C. Jung, J. H. Choi, Y. K. Han, *J. Mater. Chem. A* **2018**, *6*, 1772–1779.
- [23] X. G. Miao, R. Y. Yin, X. L. Ge, Z. Q. Li, L. W. Yin, *Small* **2017**, *13*, 1702138.
- [24] D. Sun, X. B. Zhu, B. Luo, Y. Zhang, Y. Q. Tang, H. Y. Wang, L. Z. Wang, *Adv. Energy Mater.* **2018**, *8*, 1801197.
- [25] X. W. Wang, H. P. Guo, J. Liang, J. F. Zhang, B. Zhang, J. Z. Wang, W. B. Luo, H. K. Liu, S. X. Dou, *Adv. Funct. Mater.* **2018**, *28*, 1801016.
- [26] X. Ge, Z. Li, L. Yin, *Nano Energy* **2017**, *32*, 117–124.
- [27] X. Wang, H. M. Kim, Y. Xiao, Y. K. Sun, *J. Mater. Chem. A* **2016**, *4*, 14915–14931.
- [28] H. Jiang, B. Chen, J. Pan, C. Li, C. Liu, L. Liu, T. Yang, W. Li, H. Li, Y. Wang, L. Chen, M. Chen, *J. Alloys Compd.* **2017**, *728*, 328–336.
- [29] W. Zhao, X. Ma, G. Wang, X. Long, Y. Li, W. Zhang, P. Zhang, *Appl. Surf. Sci.* **2018**, *445*, 167–174.
- [30] R. Dai, W. Sun, L. P. Lv, M. Wu, H. Liu, G. Wang, Y. Wang, *Small* **2017**, *13*, 1700521.
- [31] X. Wang, K. Chen, G. Wang, X. Liu, H. Wang, *ACS Nano* **2017**, *11*, 11602–11616.
- [32] F. Han, C. Y. J. Tan, Z. Gao, *ChemElectroChem* **2016**, *3*, 1054–1062.
- [33] D. Larcher, J. M. Tarascon, *Nat. Chem.* **2015**, *7*, 19–29.
- [34] M. M. Titirici, R. J. White, N. Brun, V. L. Budarin, D. S. Su, F. del Monte, J. H. Clark, M. J. MacLachlan, *Chem. Soc. Rev.* **2015**, *44*, 250–290.
- [35] J. Ding, H. L. Wang, Z. Li, A. Kohandehghan, K. Cui, Z. W. Xu, B. Zahiri, X. H. Tan, E. M. Lotfabad, B. C. Olsen, D. Mitlin, *ACS Nano* **2013**, *7*, 11004–11015.
- [36] B. Duan, Y. Huang, A. Lu, L. Zhang, *Prog. Polym. Sci.* **2018**, *82*, 1–33.
- [37] Z. Zhang, J. Zhang, X. Zhao, F. Yang, *Carbon* **2015**, *95*, 552–559.
- [38] F. Chen, L. Ma, J. Ren, M. Zhang, X. Luo, B. Li, Z. Song, X. Zhou, *Materials* **2018**, *11*, 989.

- [39] P. Zheng, T. Liu, X. Yuan, L. Zhang, Y. Liu, J. Huang, S. Guo, *Sci. Rep.* **2016**, *6*, 26246.
- [40] H. Li, F. Shen, W. Luo, J. Dai, X. Han, Y. Chen, Y. Yao, H. Zhu, K. Fu, E. Hitz, L. Hu, *Appl. Mater. Interfaces* **2016**, *8*, 2204–2210.
- [41] L. David, R. Bhandavat, G. Singh, *ACS Nano* **2014**, *8*, 1759–1770.
- [42] H. Zhang, I. Hasa, S. Passerini, *Adv. Energy Mater.* **2018**, *17*, DOI: 10.1002/aenm.201702582.
- [43] L. Huang, X. M. Zheng, Y. S. Wu, L. J. Xue, F. S. Ke, G. Z. Wei, S. G. Sun, *Electrochem. Commun.* **2009**, *11*, 585–588.
- [44] C. M. S. S. Mitra, *Ionics* **2013**, *20*, 137–140.
- [45] I. T. Park, H. C. Shin, *Electrochim. Commun.* **2013**, *33*, 102–106.
- [46] Y. M. Chun, H. C. Shin, *Electrochim. Acta* **2016**, *209*, 369–378.
- [47] Y. Lu, C. D. Gu, X. Ge, H. Zhang, S. Huang, X. Y. Zhao, X. L. Wang, J. P. Tu, S. X. Mao, *Electrochim. Acta* **2013**, *112*, 212–220.
- [48] F. Han, C. Zhang, J. Yang, G. Ma, K. He, X. Li, *J. Mater. Chem. A* **2016**, *4*, 12781–12789.
- [49] Z. Pu, C. Tang, Y. Luo, *Int. J. Hydrogen Energy* **2015**, *40*, 5092–5098.
- [50] X. Zhu, M. Liu, Y. Liu, R. Chen, Z. Nie, J. Li, S. Yao, *J. Mater. Chem. A* **2016**, *4*, 8974–8977.
- [51] M. Hu, L. Yang, K. Zhou, C. Zhou, Z. H. Huang, F. Kang, R. Lv, *Carbon* **2017**, *122*, 680–686.
- [52] W. Li, J. Huang, L. Feng, L. Cao, Y. Ren, R. Li, Z. Xu, J. Li, C. Yao, *J. Alloys Compd.* **2017**, *716*, 210–219.
- [53] Q. R. Yang, W. J. Li, S. L. Chou, J. Z. Wang, H. K. Liu, *RSC Adv.* **2015**, *5*, 80536–80541.
- [54] Y. Jiang, W. Zhang, Y. Yang, Y. S. He, J. Wang, X. Yang, X. Z. Liao, Z. F. Ma, *ChemNanoMat* **2018**, *4*, 309–315.
- [55] Y. Zhang, Q. Ma, S. Wang, X. Liu, L. Li, *ACS Nano* **2018**, *12*, 4824–4834.
- [56] L. Shi, D. Li, P. Yao, J. Yu, C. Li, B. Yang, C. Zhu, J. Xu, *Small* **2018**, *14*, 1802716.
- [57] T. Brezesinski, J. Wang, S. H. Tolbert, B. Dunn, *Nat. Mater.* **2010**, *9*, 146

Manuscript received: October 23, 2018

Revised manuscript received: November 24, 2018

Accepted manuscript online: November 26, 2018

Version of record online: January 11, 2019